

前所未有的终身暴露于气候极端的全球出现

<https://doi.org/10.1038/s41586-025-08907-1>

收到：2023年10月26日

接受：2025年3月17日

在线发布：2025年5月7日

开放访问

 检查更新

Luke Grant^{1,2}, Inne Vanderkelen^{1,3,4}, Lukas Gudmundsson⁵, Erich Fischer⁵, Sonia I. Seneviratne⁵和Wim Thiery¹

在人为气候变化¹下，极端气候正在升级。但是，这如何转化为一个人一生中前所未有的累积极端事件暴露尚不清楚。在这里，我们使用气候模型，影响模型和人口统计数据来投射经历累积终身暴露的人数，以高于前工业气候中预期的暴露量高于99.99%的极端。我们预计，面对这种前所未有的终身暴露于热浪，农作物故障，河流洪水，干旱，野火，野火和热带气旋的终身暴露量，从1960年到2020年将至少翻一番，并在当前的缓解政策与 2.7°C 以上的全球暖途径相一致，而Pre-c after-predy a} $^{\circ}\text{C}$ 以上的预定量为2100。1. 5°C 途径，2020年出生的人中有52%会经历前所未有的终身暴露于热浪。如果全球变暖达到 3.5°C 2100，则热浪的级数上升到92%，农作物衰竭29%，河流洪水量增加14%。在以高社会经济脆弱性为特征的人群中，面对前所未有的终身暴露的机会大大更大。我们的结果要求减少深层和持续的温室气体排放，以降低当前年轻人的气候变化负担。

极端气候对社会产生不利影响，对气候变化¹的最大关注。在热浪，河流洪水，干旱，农作物失败以及野火和热带气旋的某些方面^{2,3}中已经确定了人为影响。随着大气变暖的持续，预计其中一些事件的强度，频率和持续时间将进一步增加⁴⁻⁹，随着LEV-EL的变化，并取决于被认为³的事件。当前的策略可以将全球平均温度（GMT）加热到 $+2.7^{\circ}\text{C}$ ($+2.2\text{--}3.4^{\circ}\text{C}$) 到本世纪末¹⁰之前的工业前水平以上。由于预计这种变暖将增加人类对极端气候的暴露³，年轻一代将收获当今缓解温室气体排放的后果。

预计在当前年轻一代¹¹的一生中，上述极端极端的发生。因此，在一个人的一生中经历的极端气候极端可能远远超出了工业前气候下的预期暴露。然而，将遇到这种空前的终身暴露（ULE）的人数尚不清楚。在这里，我们通过人口统计数据，GMT轨迹和两种脆弱能力的措施，超过了气候极端的多模型投影的广泛投资组合。我们评估了ULE到极端事件的出现，以估计面对ULE的全球出生队列成员资格（方法）。然后，我们展示了如何根据脆弱性对该子人口进行分层。这是预计将在多维框架中体验ULE的人数的首次估计之一，包括出生年份，变暖场景和脆弱性。

空前接触热浪

我们说明了一个网格电池中极端热浪的含义 ($0.5^{\circ} \times 0.5^{\circ}$)，位于比利时布鲁塞尔的三种GMT途径上，在三种GMT途径中，在工业前温度上方的温度达到 1.5°C , 2.5°C 和 3.5°C and and Inluptive pation。预计他们在布鲁塞尔的生活将在他们的一生中体验三个热浪，对GMT途径几乎没有敏感性（图 1A）。在这个位置，1960年的出生队列不超过ULE的阈值，我们将其定义为前工业前控制气候中大量终生暴露的第99.99个百分点，在这里是六个热浪（图。相比之下，1990年的出生队列出现在ULE中，以显示两个最温暖的GMT路径（图 1C, D）。这意味着，在达到 2.5°C 或更高变暖的温度路径下，到2100年，该队列将面临比在没有气候变化的情况下会有一万分之一的机会所带来的热浪。不同的GMT途径在2020年在该位置出生的人的生命周期暴露导致进一步的差异（图 1E, F）。在 1.5°C 途径中，2020年出生队列预计将经历近11个热浪，但在本世纪末，这将增加到18和26热波，分别达到 2.5°C 和 3.5°C and 3.5°C 。到目前为止，这超过了每个GMT途径下的ULE阈值，在 2.5°C and 3.5°C 途径的出现年龄大约为40岁的年龄（图 1E）。然后，我们使用网格量表的绝对人口估算值来计算最终到达ULE的每个人数的人数

¹Department of Water and Climate, Vrije Universiteit Brussel, Brussels, Belgium. ²Canadian Centre for Climate Modelling and Analysis, Environment and Climate Change Canada, Victoria, British Columbia, Canada. ³Department of Earth and Environmental Sciences, KU Leuven, Leuven, Belgium. ⁴Royal Meteorological Institute Belgium, Brussels, Belgium. ⁵Institute for Atmospheric and Climate Science, ETH Zurich, Zurich, Switzerland. [✉]e-mail: luke.grant@ec.gc.ca

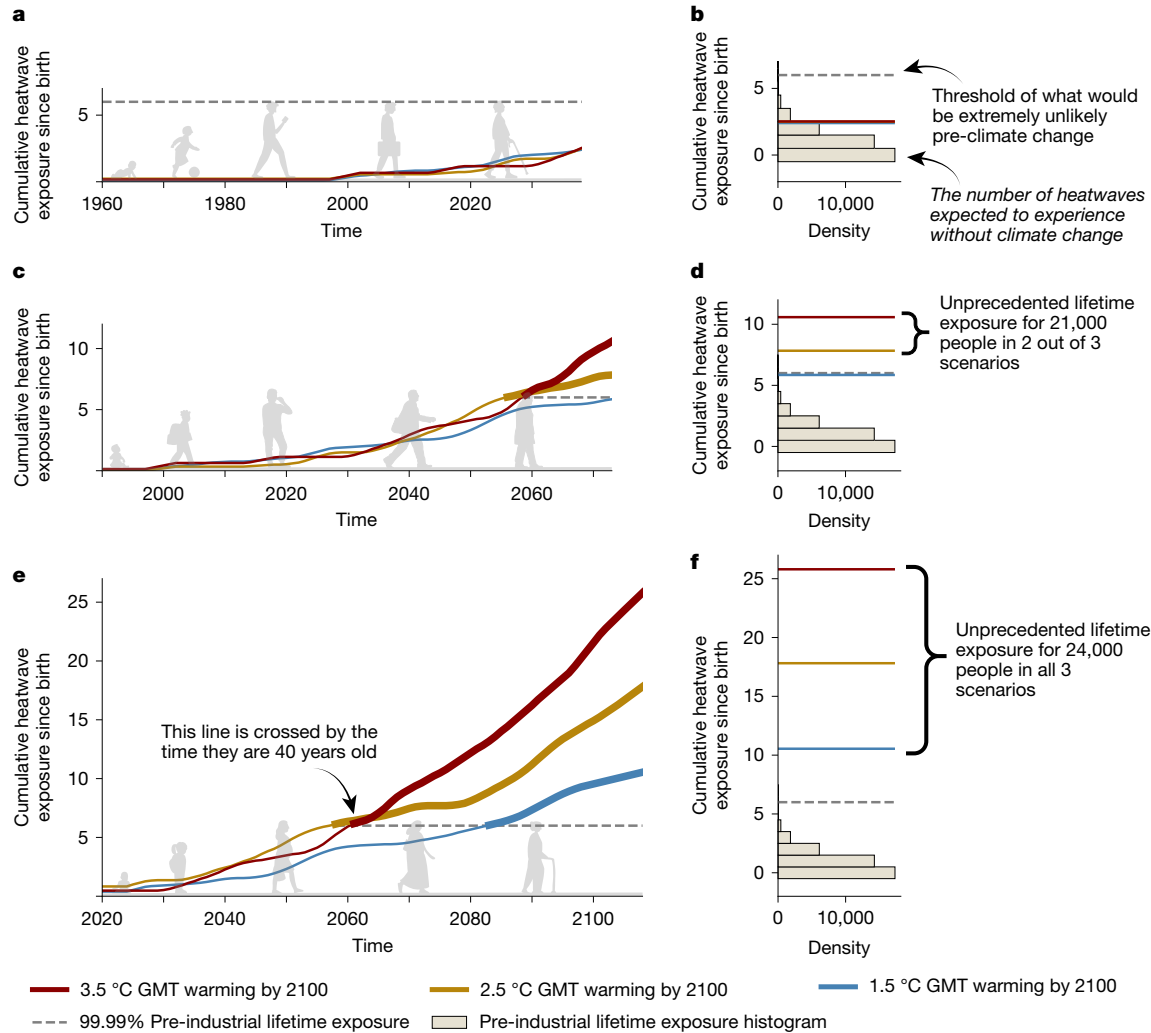


Fig. 1 | CUMULATIVE HEATWAVE EXPOSURE SINCE BIRTH FOR BRUSSELS, BELGIUM.

a,c,e, Multi-model mean time series of cumulative heatwave exposure for people born in 1960 (**a**), 1990 (**c**) and 2020 (**e**) in 1.5 °C (blue line), 2.5 °C (gold line) and 3.5 °C (red line) pathways. **b,d,f**, Histograms for 1960 (**b**), 1990 (**d**) and 2020 (**f**) birth cohorts show the pre-industrial sample density of 40,000 bootstrapped lifetime exposures overlaid with final lifetime exposures from the time series of

the birth cohort. Dashed lines show the 99.99th percentile of the pre-industrial sample distribution, that is, the threshold of unprecedented lifetime exposure (ULE) for this location, cohort and climate extreme. Counts of people (right of **d,f**) show the population of the birth cohort that has emerged beyond the 99.99th percentile of the pre-industrial sample distribution.

relative cohort sizes at the country level. In this location, a best estimate of 21,000 people from the 1990 birth cohort and 24,000 people from the 2020 birth cohort are projected to experience ULE (except for the 1990 birth cohort under the 1.5 °C pathway). Under a 1.5 °C pathway, all cohorts born in Brussels after 1990 reach ULE, totalling 665,000 people. For a 3.5 °C pathway, ULE begins for people born in 1978, increasing this total to 941,000 people. For cohorts that emerge, it is virtually certain (at least >99.99% chance) that their lifetime heatwave exposure cannot be explained by internal climate variability.

We now repeat this analysis for every land grid cell and project the population fraction of each birth cohort experiencing ULE to heatwaves across the globe ($CF_{heatwaves}$ for cohort fraction reaching ULE to heatwaves). Of the 81 million people born in 1960, on average, around 16% (13 million people) face ULE to heatwaves regardless of the scenario. This fraction rises towards younger generations, and from the 1980 birth cohort onwards, $CF_{heatwaves}$ begins to depend on GMT pathways (Fig. 2a). In a 1.5 °C pathway, $CF_{heatwaves}$ stabilizes for recent birth cohorts, reaching an average of 52% for the 2020 birth cohort (62 million people). Comparatively, $CF_{heatwaves}$ of the 2020 birth cohort is almost doubled in a 3.5 °C pathway, reaching 92%. This implies that 111 million children born in 2020 will live an unprecedented life in terms of heatwave

exposure in a world that warms to 3.5 °C compared with 62 million in a 1.5 °C pathway.

At the country level, $CF_{heatwaves}$ for the 2020 birth cohort is the highest in the tropics under low GMT pathways, yet this pattern disappears as heatwaves become widespread under high GMT pathways (Fig. 2c–e and Supplementary Tables 1–3). Under a 1.5 °C pathway, equatorial regions have relatively high $CF_{heatwaves}$; of the 177 countries in this analysis, 104 have most of the population of 2020 birth cohort living with unprecedented exposure to heatwaves ($CF_{heatwaves} \geq 50\%$; Fig. 2c). This latitudinal pattern is less apparent in a 2.5 °C pathway (Fig. 2d). Here, 157 countries have $CF_{heatwaves} \geq 50\%$. In a 3.5 °C pathway, 167 countries have $CF_{heatwaves} \geq 50\%$, 155 countries have $CF_{heatwaves} \geq 90\%$ and in 113 countries the entire birth cohort faces unprecedented heatwave exposure ($CF_{heatwaves} = 100\%$; Fig. 2e).

Unprecedented multi-hazard exposure

We then expand the analysis to a total of six climate extremes¹² and 21 warming pathways (Fig. 3 and Methods). For every combination of birth cohort, climate extreme and warming pathway, we quantify the number of people experiencing ULE at the grid scale and subsequently

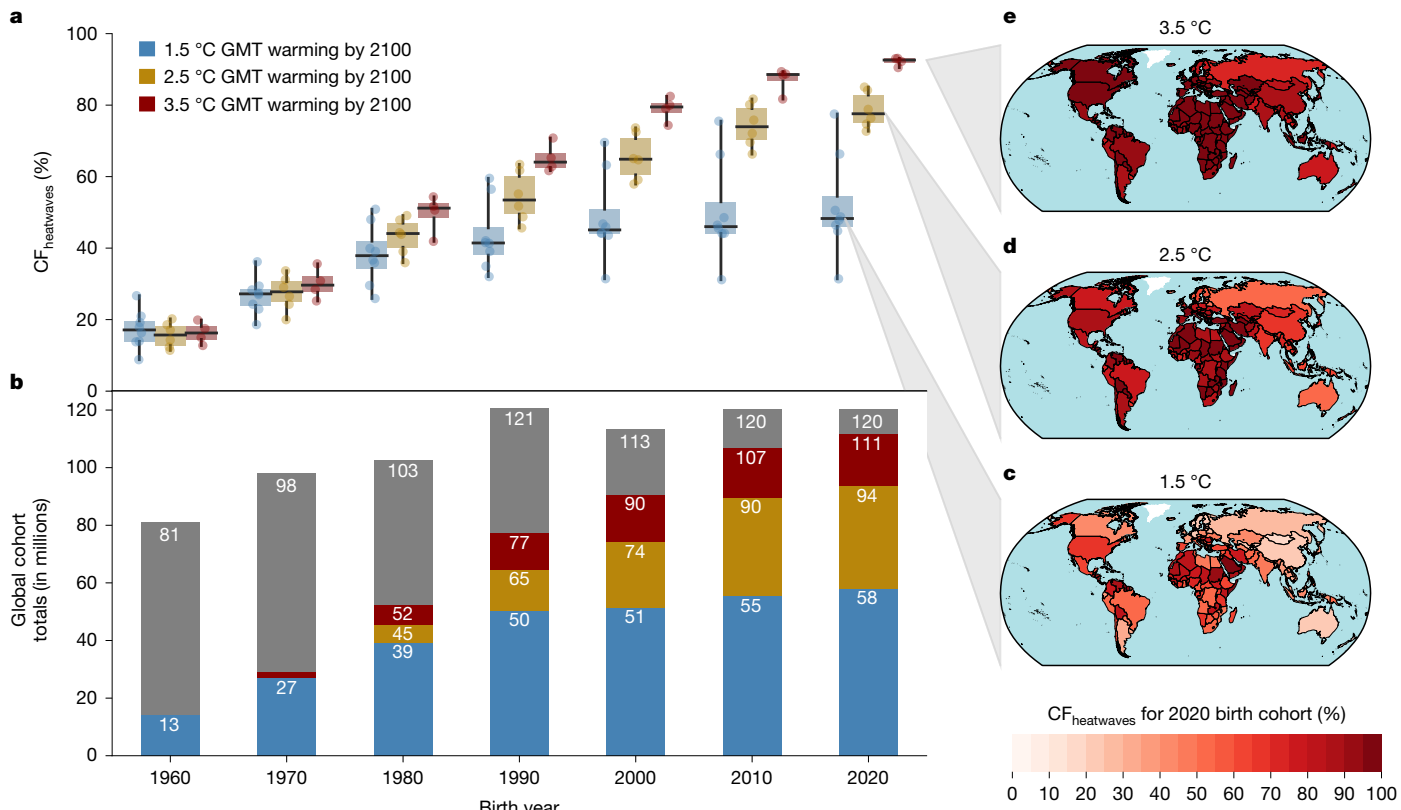


Fig. 2 | Rising fraction of birth cohorts facing unprecedented lifetime heatwave exposure. **a**, Box plots show the cohort fraction reaching ULE to heatwaves ($CF_{heatwaves}$) for 1.5 °C (blue), 2.5 °C (gold) and 3.5 °C (red) pathways for global birth cohorts between 1960 and 2020 (middle line, median; box limits, upper and lower quartiles; whiskers, extend to the full range of the

model ensemble). **b**, Bars show global cohort sizes in millions, with totals in grey and median numbers of people reaching ULE to heatwaves for 1.5 °C (blue), 2.5 °C (gold) and 3.5 °C (red) pathways. **c–e**, Maps display country-level $CF_{heatwaves}$ of the 2020 birth cohort for 1.5 °C (c), 2.5 °C (d) and 3.5 °C (e) pathways.

aggregate to the country or global level. Cohort fraction (CF) for climate extremes other than heatwaves is lower across all birth years and GMT pathways because they are generally less widespread than heatwaves; however, they still affect a large population fraction (Fig. 3 and Supplementary Tables 4–18). In a 3.5 °C pathway, 29% of those born in 2020 will live through unprecedented exposure to crop failures (Fig. 3b). This is followed by river floods, in which 14% will face unprecedented exposure to this extreme (Fig. 3e). As not all climate projections reach high warming levels, the ensemble size shrinks towards higher warming levels. Consequently, crop failures, droughts, river floods and tropical cyclones, which are more dependent on changes in the water cycle than heatwaves, exhibit discontinuities in CF at some GMT intervals (Fig. 3b,d–f). These sampling artefacts disappear when visualizing CFs for a smaller subset of simulations that are available for all GMT trajectories (Supplementary Note 1 and Supplementary Fig. 1). Although model uncertainties are larger for extremes other than heatwaves, differences in CF across birth cohorts are statistically significant for all six climate extremes (Supplementary Note 2 and Supplementary Figs. 2 and 3).

Across all projections available for the 2.7 °C pathway aligned with current policies¹⁰, ULE to heatwaves occurs in the Americas, Africa, the Middle East and Australia already for the 1960 birth cohort and globally for the 2020 birth cohort (Supplementary Figs. 4m–o and 5e,k). The ULE to crop failures expands around the United States, South America, Sub-Saharan Africa and East Asia between 1960 and 2020 cohorts (Supplementary Figs. 4 and 5b,h). The ULE to river floods occurs in northern latitudes for the 1960 cohort, in line with the observations and model projections for precipitation changes^{13–15} and expands southwards into much of the world for the 2020 cohort (Supplementary Fig. 5d,j).

The lower CF of some extremes, such as tropical cyclones, is expected given the geographical constraints of these events and their distinct meteorological drivers. Tropical cyclones can, therefore, be re-evaluated by limiting the analysis to regions that can experience them. We consider these regions to be any grid cells exposed at least once to the event across our whole ensemble of exposure projections (Supplementary Fig. 6). $CF_{tropical\ cyclones}$ nearly doubles when constraining total birth cohort size to exposed regions. For the 2020 birth cohort, this estimate changes from 6% to 11% in a 1.5 °C pathway and from 10% to 19% in a 3.5 °C pathway.

Heatwaves across vulnerability strata

Finally, we cross our grid-scale projections for ULE to heatwaves against two grid-scale indicators of socioeconomic vulnerability (Methods): (1) the Global Gridded Relative Deprivation Index v.1 (GRDI; ref. 16), which expresses relative deprivation according to six socioeconomic indicators; and (2) lifetime mean GDP per capita (denoted as GDP; ref. 17). Binning our birth cohort members into the top and bottom 20% of GRDI (Fig. 4a) and GDP (Supplementary Fig. 7a) enables a grid-scale comparison of ULE for population groups with high and low socioeconomic vulnerability. Using GRDI, we find that the most vulnerable subset of each birth cohort projected to experience ULE to heatwaves under current policies is substantially larger than the least vulnerable subset. This implies that socioeconomically vulnerable people have a consistently higher chance of facing unprecedented lifetime heatwave exposure compared with the least vulnerable members of their generation (Fig. 4b). For example, of the 2020 birth cohort, 95% or 23 million members of the high deprivation (high socioeconomic vulnerability)

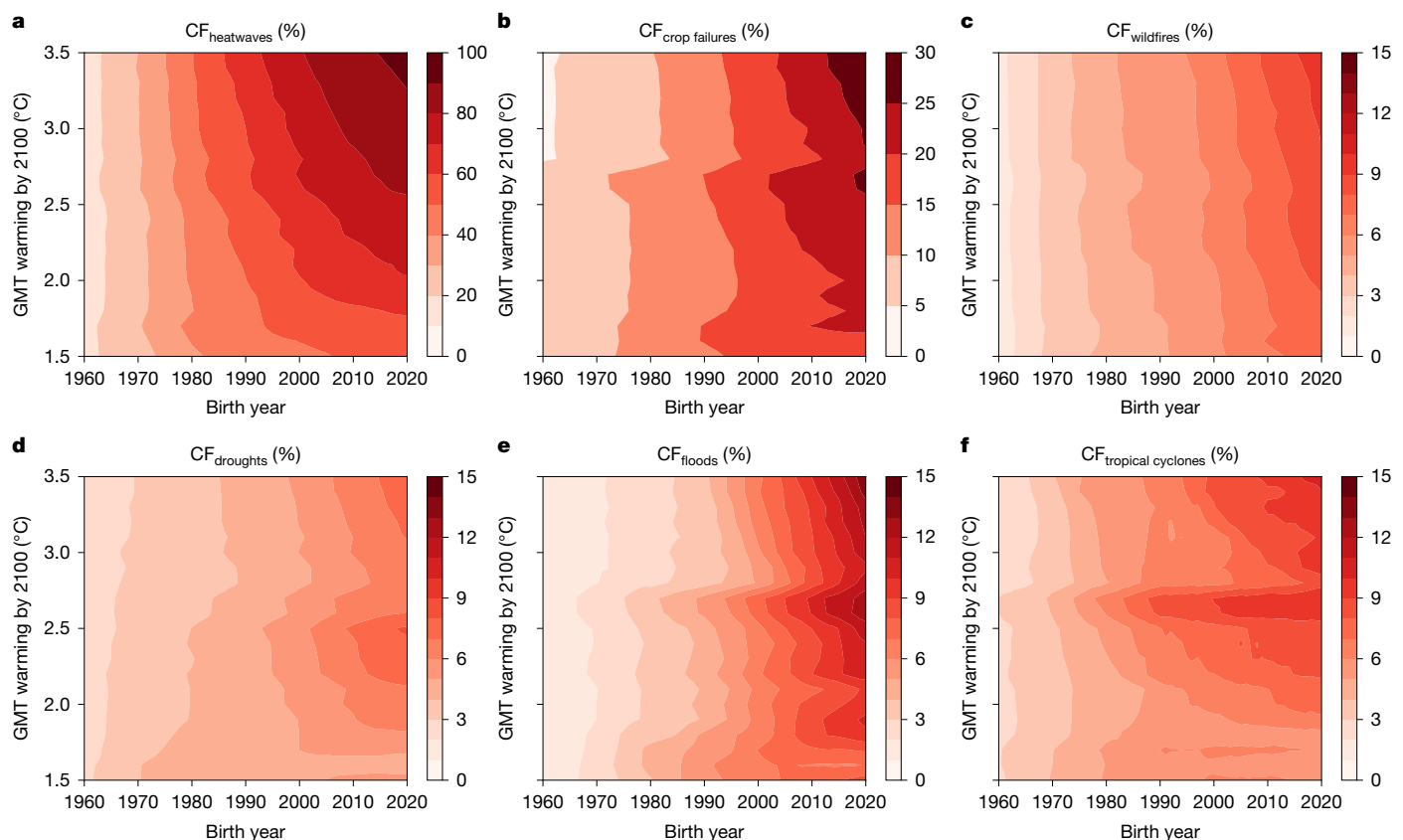


Fig. 3 | Greater unprecedented exposure to climate extremes for younger generations and higher warming pathways. **a–d**, Cohort fraction (CF) across all birth years (1960–2020) and GMT pathways (1.5–3.5 °C) for heatwaves

(CF_{heatwaves}; **a**), crop failures (CF_{crop failures}; **b**), wildfires (CF_{wildfires}; **c**), droughts (CF_{droughts}; **d**), river floods (CF_{floods}; **e**) and tropical cyclones (CF_{tropical cyclones}; **f**). Each extreme event panel has its colour bar range.

group face ULE to heatwaves, whereas this is 78% (19 million) for the low deprivation group. This disparity is similar when using GDP, but with only 1974 and later birth years having significant differences across vulnerability strata (Supplementary Fig. 7). Here, for the 2020 birth year, 92% (22 million) of the low-income group face ULE under current policies, whereas this is 79% (19 million) for the high-income group. Under alternative warming pathways of 1.5 °C and 3.5 °C, although the same direction of disparities remains across vulnerability strata, the lowest vulnerability groups (low deprivation and high GDP) benefit the most from a low warming pathway (Fig. 4c,d and Supplementary Fig. 7c,d). Socioeconomically vulnerable groups have lower adaptive capacity and face more constraints when it comes to implementing effective adaptation measures^{18,19}. Our results highlight that precisely these groups with the highest socioeconomic vulnerability and lowest adaptation potential face the highest chance for unprecedented heatwave exposure (Fig. 4). This underlines the disproportionate risk for deprived communities in light of past and future climate extremes.

Discussion

Our analysis only quantifies local exposure by design; yet in reality, the effects of climate extremes cascade non-locally. For example, in 2023, smoke from an active wildfire season in Canada was transported south along the east coast of the United States, exposing millions of people to hazardous air quality²⁰ and causing an increased cardiopulmonary disease burden²¹. Climate extremes also affect society through economic impacts, including the rising cost of living due to supply chain disruptions²² and taxation to recover public infrastructure²³. For instance, climate change endangers staple crop production in

the main breadbasket countries that supply most of our caloric intake globally²⁴, forcing market instabilities that only the wealthiest can cope with²⁵. These missing non-local impacts make our estimates conservative.

By contrast, we do not capture how people adapt to extremes and thereby potentially reduce their exposure or vulnerability. For example, exposure to heatwaves can be reduced for population groups that can afford access to air conditioning¹⁸. However, maladaptive responses to climate extremes can instead create lock-ins of vulnerability and exposure¹. Therefore, our lifetime exposure estimates omit beneficial adaptation outcomes as well as detrimental non-local and maladaptation effects. Finally, opting for a threshold below 99.99% would lower the bar and increase ULE estimates, and vice versa. Yet this effect is limited because the reference distribution is typically composed of small integers. By contrast, using thresholds above 99.99% risks redundancy in our bootstrapped data sample (Methods).

Some demographic realities are not accounted for here. Factors such as within-country migration, fertility and mortality respond in reality to the climate extremes considered here¹¹. In the United States, where the population faces exposure to all extremes analysed in this study, city centres attract young people²⁶ and disparities in life expectancy have been found across race–county combinations²⁷ and rural–urban residency²⁸. For instance, life expectancy is longer for those living in cities, yet here we apply country-average life expectancy and cohort size distribution uniformly within each country. Furthermore, we do not account for within-grid-cell heterogeneity, that is, we miss some fine-scale variations in socioeconomic vulnerability and exposure in socioeconomically diverse regions such as cities. Finally, we focus on the socioeconomic dimension of vulnerability,

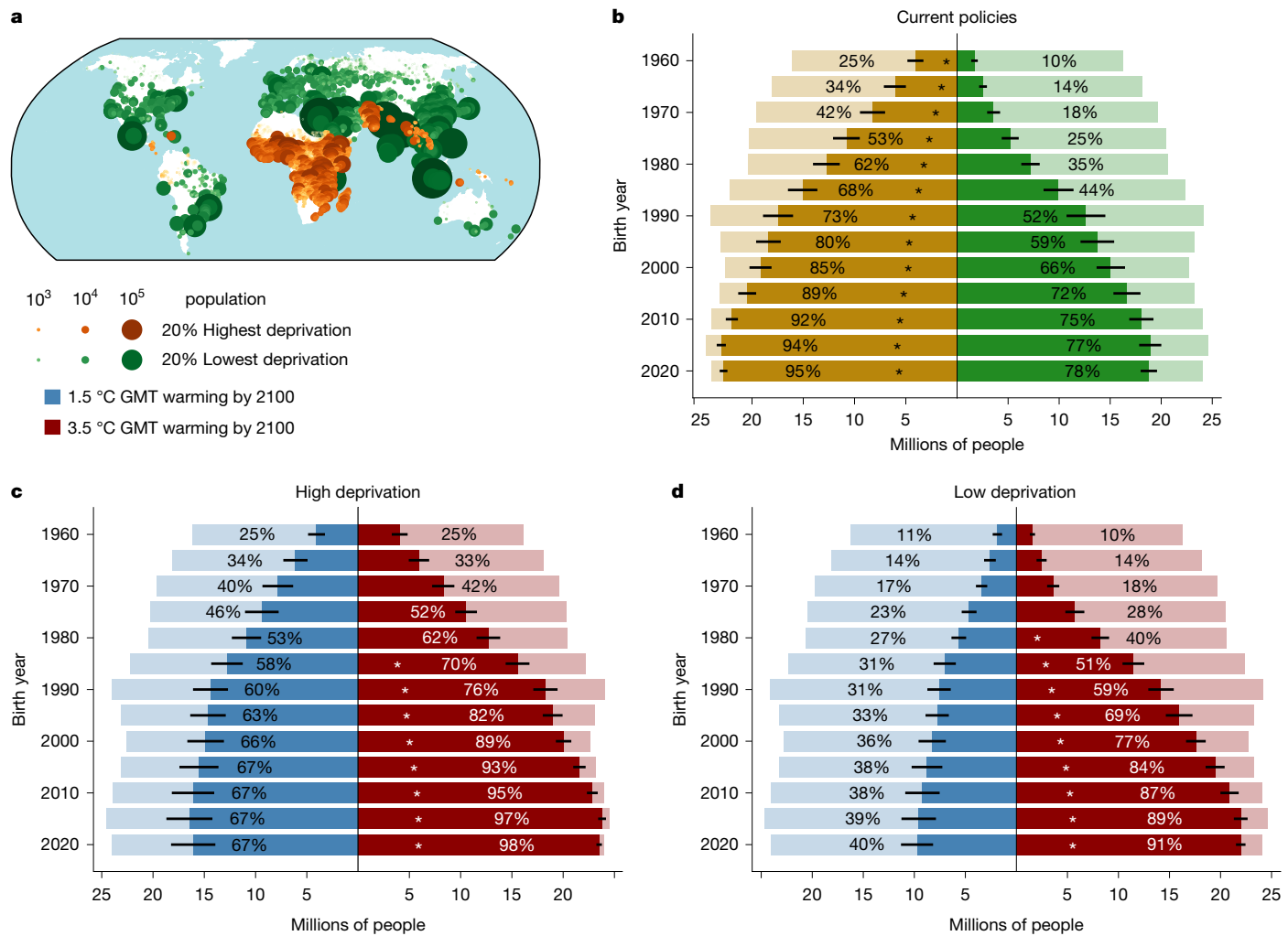


Fig. 4 | The most deprived face significantly higher chance of ULE to heatwaves. **a**, Geographic distribution of the 20% highest (brown markers) and 20% lowest (green markers) scoring 2020 birth cohort members (with roughly equal population) in the GRDI¹⁶. Grid cell marker sizes and colours are scaled by their population. **b**, Fraction of these two groups projected to experience ULE to heatwaves under the current policies pathway of 2.7 °C warming by 2100 for every fifth birth year. Light-coloured bars show total cohort sizes per birth year

and vulnerability group, whereas dark colours indicate the affected fraction. Error bars show the standard deviation across projections. Asterisks indicate that a low- or high-vulnerability group from a given birth cohort has significantly more members with ULE to heatwaves than the alternative vulnerability group of the same birth cohort (at the 5% level). **c,d**, The high deprivation (**c**) and low deprivation (**d**) share of the birth cohort that is projected to experience ULE under the 1.5 °C (blue) and 3.5 °C (red) pathways.

thereby neglecting that vulnerability to climate extremes may also vary with, for instance, age, gender or disability status. As demographic and multidimensional vulnerability information becomes available at ever higher spatial resolution and explicitly accounts for climate impact projections, it will become possible to deepen the analysis of the interaction between climate change and population dynamics.

The uncertainties of the extremes other than heatwaves are non-negligible. Hydrological variables have high internal climate variability²⁹ and projecting these events requires an additional impact-modelling step relative to heatwaves, which are computed directly from global climate model output (Methods). Furthermore, these events have sensitivities to input data quality and process representation across the modelling chain (Supplementary Note 2). Other uncertainties, such as demographic representation, are not captured in this analysis. Finally, we opt for assessing ULE at the grid scale instead of at the country level. In doing so, we downscale demographic data instead of upscaling climate data, thereby projecting lifetime exposure based on the local climate of individual birth cohort members. This incurs a trade-off for accepting natural variability in locations at

which ULE occurs, yet minimizing year-to-year variability in country- and global-scale CF estimates (Supplementary Note 3 and Supplementary Fig. 8).

Conclusions

In summary, we find that large fractions of global birth cohorts are projected to live unprecedented exposure to heatwaves, river floods, droughts, crop failures, wildfires and tropical cyclones. As the frequency of these six climate extremes increases with warming, so does the fraction of people who will face ULE to these events. More ambitious policies are needed to achieve the goal of the Paris Agreement of limiting global warming to 1.5 °C by 2100 relative to the 2.7 °C warming expected under current policies, especially as the most vulnerable groups have more members projected to face unprecedented exposure to heatwaves. Children would reap the direct benefits of this increased ambition: a total of 613 million children born between 2003 and 2020 would then avoid ULE to heatwaves. For crop failures, this is 98 million, for river floods 64 million, for tropical cyclones 76 million, for droughts 26 million and for wildfires 17 million. This underlines the urgent need

for deep and sustained greenhouse gas emission reductions to safeguard the future of current young generations.

Online content

Any methods, additional references, Nature Portfolio reporting summaries, source data, extended data, supplementary information, acknowledgements, peer review information; details of author contributions and competing interests; and statements of data and code availability are available at <https://doi.org/10.1038/s41586-025-08907-1>.

1. IPCC. *Climate Change 2022: Impacts, Adaptation and Vulnerability. Contribution of Working Group II to the Sixth Assessment Report of the Intergovernmental Panel on Climate Change* (Cambridge Univ. Press, 2022).
2. Burton, C. et al. Global burned area increasingly explained by climate change. *Nat. Clim. Change* **14**, 1186–1192 (2024).
3. Seneviratne, S. I. et al. in *Climate Change 2021: The Physical Science Basis. Contribution of Working Group I to the Sixth Assessment Report of the Intergovernmental Panel on Climate Change* (eds Masson-Delmotte, V. et al.) (Cambridge Univ. Press, 2021).
4. Cook, B. I. et al. Twenty-first century drought projections in the CMIP6 forcing scenarios. *Earth's Future* **8**, 2019–001461 (2020).
5. Domeisen, D. I. V. et al. Prediction and projection of heatwaves. *Nat. Rev. Earth Environ.* **4**, 36–50 (2023).
6. Gaupp, F., Hall, J., Mitchell, D. & Dadson, S. Increasing risks of multiple breadbasket failure under 1.5 and 2°C global warming. *Agric. Syst.* **175**, 34–45 (2019).
7. Yu, Y. et al. Machine learning-based observation-constrained projections reveal elevated global socioeconomic risks from wildfire. *Nat. Commun.* **13**, 1250 (2022).
8. Hirabayashi, Y. et al. Global flood risk under climate change. *Nat. Clim. Change* **3**, 816–821 (2013).
9. Knutson, T. R. et al. Tropical cyclones and climate change. *Nat. Geosci.* **3**, 157–163 (2010).
10. Climate Action Tracker. *The CAT Thermometer*. <https://climateactiontracker.org/global/cat-thermometer> (2022).
11. Thiery, W. et al. Intergenerational inequities in exposure to climate extremes. *Science* **374**, 158–160 (2021).
12. Lange, S. et al. Projecting exposure to extreme climate impact events across six event categories and three spatial scales. *Earth's Future* **8**, e2020EF001616 (2020).
13. Wan, H., Zhang, X., Zwiers, F. & Min, S.-K. Attributing northern high-latitude precipitation change over the period 1966–2005 to human influence. *Clim. Dyn.* **45**, 1713–1726 (2015).
14. Knutson, T. R. & Zeng, F. Model assessment of observed precipitation trends over land regions: detectable human influences and Possible low bias in model trends. *J. Clim.* **31**, 4617–4637 (2018).
15. Wang, Y. et al. Influence of anthropogenic and natural forcings on future changes in precipitation projected by the CMIP6-DAMIP models. *Int. J. Climatol.* **43**, 3892–3906 (2023).
16. Center for International Earth Science Information Network-CIESIN-Columbia University. *Global Gridded Relative Deprivation Index (GRDI), Version 1* (NASA Socioeconomic Data and Applications Center, 2022).
17. Frieler, K. et al. Assessing the impacts of 1.5°C global warming – simulation protocol of the Inter-Sectoral Impact Model Intercomparison Project (ISIMIP2b). *Geosci. Model Dev.* **10**, 4321–4345 (2017).
18. Andrijevic, M., Byers, E., Mastrucci, A., Smits, J. & Fuss, S. Future cooling gap in shared socioeconomic pathways. *Environ. Res. Lett.* **16**, 94053 (2021).
19. Andrijevic, M. et al. Towards scenario representation of adaptive capacity for global climate change assessments. *Nat. Clim. Change* **13**, 778–787 (2023).
20. Jain, P. et al. Drivers and impacts of the record-breaking 2023 wildfire season in Canada. *Nat. Commun.* **15**, 6764 (2024).
21. Maldarelli, M. E. et al. Polluted air from Canadian wildfires and cardiopulmonary disease in the Eastern US. *JAMA Netw. Open* **7**, 2450759–2450759 (2024).
22. Franzke, C. L. E. Impacts of a changing climate on economic damages and insurance. *Econ. Disasters Clim. Change* **1**, 95–110 (2017).
23. Cigler, B. A. U.S. floods: the necessity of mitigation. *State Local Gov. Rev.* **49**, 127–139 (2017).
24. Caparas, M., Zobel, Z., Castanho, A. D. A. & Schwalm, C. R. Increasing risks of crop failure and water scarcity in global breadbaskets by 2030. *Environ. Res. Lett.* **16**, 104013 (2021).
25. Tigchelaar, M., Battisti, D. S., Naylor, R. L. & Ray, D. K. Future warming increases probability of globally synchronized maize production shocks. *Proc. Natl. Acad. Sci. USA* **115**, 6644–6649 (2018).
26. Lee, Y., Lee, B. & Shubro, M. T. H. Urban revival by millennials? Intraurban net migration patterns of young adults, 1980–2010. *J. Reg. Sci.* **59**, 538–566 (2019).
27. Murray, C. J. L. et al. Eight Americas: investigating mortality disparities across races, counties, and race-counties in the United States. *PLoS Med.* **3**, 1513–1524 (2006).
28. Singh, G. K. & Siahpush, M. Widening rural–urban disparities in life expectancy, U.S., 1969–2009. *Am. J. Prev. Med.* **46**, e19–e29 (2014).
29. Douville, H. et al. in *Climate Change 2021: The Physical Science Basis. Contribution of Working Group I to the Sixth Assessment Report of the Intergovernmental Panel on Climate Change* (eds Masson-Delmotte, V. et al.) (Cambridge Univ. Press, 2021).

Publisher's note Springer Nature remains neutral with regard to jurisdictional claims in published maps and institutional affiliations.



Open Access This article is licensed under a Creative Commons Attribution 4.0 International License, which permits use, sharing, adaptation, distribution and reproduction in any medium or format, as long as you give appropriate credit to the original author(s) and the source, provide a link to the Creative Commons licence, and indicate if changes were made. The images or other third party material in this article are included in the article's Creative Commons licence, unless indicated otherwise in a credit line to the material. If material is not included in the article's Creative Commons licence and your intended use is not permitted by statutory regulation or exceeds the permitted use, you will need to obtain permission directly from the copyright holder. To view a copy of this licence, visit <http://creativecommons.org/licenses/by/4.0/>.

© Crown 2025

Article

Methods

ISIMIP and exposure projections

The Inter-Sectoral Impact Model Intercomparison Project (ISIMIP) provides a simulation protocol for projecting the impacts of climate change across sectors such as biomes, agriculture, lakes, water, fisheries, marine ecosystems and permafrost (www.isimip.org). In ISIMIP2b, impact models representing these sectors are run using atmospheric boundary conditions from a consistent set of bias-adjusted global climate models (GCMs) from phase 5 of the Coupled Model Intercomparison Project (CMIP5) that were selected based on their availability of daily data and ability to represent a range of climate sensitivities¹⁷; the Geophysical Fluid Dynamics Laboratory Earth System Model (GFDL-ESM2M; ref. 30), the earth system configuration of the Hadley Centre Global Environmental Model (HadGEM2-ES; ref. 31), the general circulation model from the Institut Pierre-Simon Laplace Coupled Model (IPSL-CM5A-LR; ref. 32) and the Model for Interdisciplinary Research on Climate (MIROC5; ref. 33). Impact simulations are run for pre-industrial control (286 ppm CO₂; 1666–2099), historical (1861–2005) and future (2006–2099) periods. Future simulations are based on Representative Concentration Pathways (RCPs) 2.6, 6.0 and 8.5 of GCM input datasets. Global projections of annual, grid-scale fractions of exposure to each extreme event category are calculated from ISIMIP2b impact simulations and GCM input data. For the full details of these computations, we refer to ref. 12, but we summarize extreme event definitions below.

For heatwaves, droughts, crop failures and river floods, we use localized pre-industrial thresholds to determine event occurrences, whereas for tropical cyclones, we use a single absolute threshold, and wildfires are modelled explicitly (Supplementary Table 20). Heatwaves affect an entire grid cell if the Heat Wave Magnitude Index daily (HWMid; refs. 34,35) of that year exceeds a threshold in the pre-industrial control HWMid distribution in that grid cell¹¹. Although we refer to heatwaves throughout the paper, our definition technically refers to a 3-day extreme heat event that is expected on average once per century under pre-industrial climate conditions. These extreme heat events occur, by definition, everywhere across the world, but with different associated absolute temperature values. Previous analysis highlighted that intergenerational inequalities in lifetime heatwave exposure are robust across a range of heatwave definitions¹¹. Crop failures are based on the sum of the area occupied by maize, wheat, soy or rice within a grid cell when their simulated yield falls below a threshold of their pre-industrial reference yield. Droughts, such as heatwaves, affect an entire grid cell if, for 7 months, monthly soil moisture remains below a threshold of pre-industrial soil moisture levels. Floods only correspond to river flooding, and the flooded area is derived from comparing daily discharge simulations from models of the global water sector to pre-industrial discharge. CaMa-Flood, a global river-routing model³⁶, is used to convert these discharge values to flooded areas. Tropical cyclones occur if a grid cell sustains hurricane-force winds (≥ 64 knots) at least once a year^{37,38}. Exposure to tropical cyclones does not encompass the flood hazards typically associated with tropical cyclones. Wildfires occur when the burnt area is simulated in a grid cell. Burnt area is either taken directly from annual burnt area calculations or as the annual sum of monthly burnt area in cases in which impact models simulate burnt area sub-annually, capped at 100% of a grid cell. We reiterate that all exposure definitions here neglect potential exposure reduction measures and non-local effects.

We subsequently quantify human exposure to climate extremes in a way that facilitates comparison and aggregation across extreme event categories. We consider all people in a grid cell exposed to a climate extreme in a particular year if the climate extreme occurs in that year. We thereby assume that if such a river flood or wildfire occurs somewhere in a $0.5^\circ \times 0.5^\circ$ grid cell, this is sufficiently close to any person located in that grid cell to be considered affected by this extreme

event. Using demographic data (see below), we subsequently convert this annual human exposure to lifetime exposure of birth cohorts by summing annual grid fractions of individual event categories across their lifetimes.

Demographics

Demographic data for population totals, cohort sizes and life expectancy enable our projection of the CF experiencing ULE to these six extremes. Population totals at the grid scale come from the ISIMIP database (Fig. 2b; ref. 17) and originate from population estimates from v.3.2 of the History Database of the Global Environment (HYDE3.2; refs. 39,40) for the historical period (1860–2000) and population projections from middle-of-the-road Shared Socioeconomic Pathway (SSP2; refs. 41,42) for the future period (2010–2100). We note that these datasets at present do not account for the impact of climate on population dynamics, for example, through changes in migration, fertility and mortality, although these feedbacks may substantially alter the demographic data. Cohort sizes from the Wittgenstein Centre for Demography and Global Human Capital⁴³ provide estimates of country-level population totals every 5 years (between 1950 and 2100) for each 5-year age group (0- to 4-year-olds, 5- to 9-year-olds, and so on, until 95- to 99-year-olds and a final age group for those 100 years and older). Life expectancy data come from the United Nations World Population Prospects (UNWPP; ref. 44) and describe the life expectancy of 5-year-olds at the country level for 5-year blocks (1950–1955 to 2015–2020). In this dataset, life expectancy is reported for 5-year-olds to exclude biases from infant mortality. Countries that can be spatially resolved at the ISIMIP grid scale and have cohort and life expectancy estimates in these datasets meet the requirements of this study and total 177. We refer to the supplementary material of ref. 11 for a broader discussion of these datasets but explain our application of them in this analysis below.

All demographic datasets are modified to represent lifetimes annually, beginning from 1960 to 2020. Life expectancies for each country are first linearly interpolated to annual values by assuming that the values of the original 5-year groups are representative of the middle of that group. Furthermore, we add 5 years to annual life expectancies to capture the life expectancy of each cohort since birth, as the original data begin at age 5. As the maximum UNWPP life expectancy for people born in 2020 prescribes the final year in this analysis (2113), annual population totals must be extrapolated to reach this year. For population totals, we take each year beyond 2100 as the mean of the preceding 10 years of the dataset, such that population numbers for 2101 are the mean of 2091–2100. For cohort sizes in each country, we interpolate annual cohort sizes and age groups from the original 5-year age groups and divide age totals by 5 to maintain original population sizes in this dataset and linearly extrapolate these estimates to 2113. This provides the absolute numbers of 0- to 100-year-olds for each year across 1960–2113.

To downscale this demographic information to the grid scale, we assume spatially homogeneous cohort representation and life expectancy. Birth cohort size is represented as the number of people of age 0 of a given birth year in a given grid cell. This is estimated by multiplying the absolute population of the birth year (using the annual grid-scale population totals from ISIMIP) by the relative size of the age 0 cohort (using the interpolated 0- to 100-year-old population totals from the Wittgenstein Centre cohort data). Spatial variability in age structure and life expectancy within a country is therefore ignored in this study.

Mapping impacts to GMT trajectories

To project CF across different warming pathways by 2100, we construct a series of incrementally warming GMT pathways between 1960 and 2113 based on GMT trajectories taken from the AR6 Scenario Explorer⁴⁵. The time series from the AR6 scenario explorer were chosen as anchor points for interpolation to produce a range of plausible GMT time series. Furthermore, they were selected to minimize overshooting in the early

years of low GMT pathways over higher GMT pathways, which can skew lifetime exposure estimates for early birth cohorts (Supplementary Fig. 9). The upper bound of this subset was limited to 3.5 °C in favour of sampling more simulations for higher GMT projections, which we discuss further below. For the lower bound, 1.5 °C was chosen because it is a more realistic minimal warming scenario than 1.0 °C. Note that the 1.5 °C anchor scenario maximally reaches 1.57 °C before reducing to 1.5 °C by 2100. It is, therefore, referred to as 1.5 °C throughout this analysis. These warming levels are reported relative to pre-industrial temperatures from 1850 to 1900. This yields a total of 21 GMT pathways for which we project CF.

Our dataset of extreme event exposures represents occurrences of these extremes forced by GCM-modelled climates. These climates have unique GMT warming pathways that depend on their radiative forcing scenario (historical or RCP), as prescribed by the ISIMIP2b modelling protocol. To project these exposure maps along even intervals of warming scenarios, which the original simulations do not provide, we use the 21 GMT pathways described above. For each pairing of the 21 target GMT pathways and the concatenated historical and future exposure projections, we sample exposures by matching the GMT warming levels of the exposure series to the years of the target GMT pathways (Supplementary Figs. 9 and 10). The GMT warming levels behind the exposure projections are first smoothed with a 21-year rolling mean before GMT mapping is undertaken. In cases in which our constructed GMT pathways exceed the GMT warming levels of GCM simulations by too much, this mapping erroneously resamples the year of exposures corresponding to the maximum warming level of their forcing GCM. To this end, we implement a constraint in this sampling procedure such that GMT-mapped series are only used if the maximum difference across all GMT pairs is no larger than 0.2 °C. This constraint incrementally reduces ensemble sizes of exposure projections for higher GMT pathways (Supplementary Table 19).

Lifetime exposure

Estimating lifetime exposure to extreme events requires crossing life expectancy data at the country level with grid-scale exposure projections. For each GMT trajectory (1.5–3.5 °C, 0.1 °C intervals), birth year (1960–2020) and country (177), exposures are summed across lifetimes at the grid scale. This assumes life expectancy to be spatially homogeneous across each country. Exposure during the death years is also included in this sum by multiplying these exposure projections by the fraction of the final year lived. This produces country-wide maps of lifetime exposure at the grid scale for each GMT trajectory and birth year in this analysis.

To generate a baseline distribution of lifetime exposure in a world without climate change, large samples of pre-industrial lifetime exposures are bootstrapped assuming 1960 life expectancy in each country. Here, for each exposure projection originating from a simulation under a pre-industrial climate, 10,000 lifetime exposures are estimated by resampling exposure years with replacement. Depending on ISIMIP2b data availability, pre-industrial exposure projections have a length of 239–639 years per simulation from which to resample from¹¹. This process generates 40,000–310,000 country-wide maps of lifetime exposure, depending on the extreme event considered and its underlying data availability, enabling exposure projections in a pre-industrial climate. Using the pre-industrial period as a baseline enables (1) our GMT mapping procedure; (2) bootstrapping a stationary time series to achieve a large reference dataset; and (3) the production of a reference dataset with information that is independent of the projections forming our ULE estimates.

Emergence of ULE

We define an emergence threshold for ULE to extreme events as the 99.99th percentile of our grid-scale samples of pre-industrial lifetime exposure. When it comes to the selection of this percentile, we went

as extreme as possible given the bootstrapping of the pre-industrial control runs. This choice was based on a sensitivity analysis for different percentile values that showed a levelling off of lifetime exposure for percentiles more extreme than 99.99%. This indicated that the 99.99th percentile achieves the limit of reliable information that can be extracted from the empirical distribution. For each extreme event, birth year, GMT pathway and grid cell, we assess if lifetime exposure emerges or passes this threshold of extreme exposure in a pre-industrial climate. If this threshold is passed, we consider the whole birth cohort in this grid cell to have emerged, tallying its size among a global pool of the same birth cohort and GMT trajectory of people projected to live ULE. This means that, in some locations, even if the sum of exposed grid cell fractions across a pre-industrial lifetime does not cover the entire grid cell, we still extract the entire birth cohort size associated with that grid cell. We sum the number of emerged people in each birth cohort globally, although this birth cohort has a different life expectancy in each country. Once the number of people who have emerged globally is tallied, we divide this by the respective total cohort sizes to estimate CF per birth cohort. Note that ULE, therefore, does not refer to unprecedented in terms of the magnitude of assets or people exposed, but rather in terms of the number of events accumulated across an average person's lifespan in comparison with what they would face in a pre-industrial climate.

ULE across socioeconomic vulnerability strata

We use two grid-scale indicators of vulnerability to compare with our estimates of ULE to heat waves. The first is an ISIMIP2b GDP input dataset using concatenated historical and SSP2 time series covering 1860–2099 annually¹⁷. This dataset was disaggregated from the country to grid level using spatial and socioeconomic interactions among cities, land cover and road network information and SSP-prescribed estimates of rural and urban expansion⁴⁶. The second indicator is the Global Gridded Relative Deprivation Index v.1 (GRDI; ref. 16), which communicates relative levels of multidimensional deprivation and poverty (0–100, least to most deprived). This deprivation score uses six input components. First is the child dependency ratio, which is the ratio between the population of children and the working-age population (15–64 years). This can indicate vulnerability, for which high ratios indicate a dependency of supposed consumers and non-producers on the working-age (producing) population⁴⁷. Second, infant mortality rates (IMR), taken as the deaths in children younger than 1 year of age per 1,000 live births annually, are a signal of population health and form a long-term Sustainable Development Goal of the United Nations⁴⁸. Third, the Subnational Human Development Index (SHDI), an assessment of human well-being across education, health and standard of living, originates from the Human Development Index, the latter of which is considered one of the most popular indices to assess country-level well-being. The SHDI improves on the HDI in terms of spatial scale and in representing 161 countries across all world regions and development levels⁴⁹. Fourth, as rural populations are generally prone to multidimensional poverty⁵⁰, low values in the ratio of built-up to non-built-up area (BUILT) signal high deprivation. The fifth and sixth components use the mean (of 2020; VNL 2020) and slope (2012–2020; VNL Slope) of nighttime light intensity, a proxy for human activity, economic output and infrastructure development⁵¹, to indicate deprivation for areas of low nighttime light intensity. These input components range from 30 arc seconds (roughly 1 km) resolution to subnational regions and are harmonized in an ArcGIS Fishnet feature class for aggregation onto a 0–100 range representing low to high deprivation. For the final aggregation, the IMR and SHDI components are given half the weight of the rest of the inputs, given their coarser resolution. The GRDI, therefore, encapsulates multiple dimensions through which generations face deprivation and therewith socioeconomic vulnerability to climate extremes. Although our approach does not explicitly account for actual or potential adaptation to climate change, this multidimensional approach to

Article

vulnerability provides relevant information on the current adaptation potential of local populations.

We preprocess GDP and GRDI products to enable their comparison with our ULE estimates across birth years. For GDP, similar to other datasets in our analysis, we extend the series to 2113 to accommodate the longest life expectancy of the 2020 birth cohort by copying the final year of the original dataset. We then use our ISIMIP population totals to compute GDP per capita at the grid scale. Using the GDP per capita metric, we calculate lifetime mean GDP per capita using our life expectancy information for the 1960–2020 birth cohorts. We refer to lifetime mean GDP per capita as simply GDP. For GRDI, we conservatively regrid the original grid cells of about 1 km to the 0.5° ISIMIP grid. Although GRDI is a map composed of data spanning 2010–2020, we assume this to be representative of 2020, but nonetheless compare it with the 1960–2020 birth cohort range, similar to the rest of the analysis.

We then identify 20% quantile ranges (that is, (0–20], (20–40], ..., (80–100]) for the lifetime GDP of each birth year and for the singular GRDI map (assumed to align with 2020 population totals). To this end, we rank the vulnerability indicators and apply these ranks to our birth cohort totals on the same grid and for the matching year. For example, the ranks taken from the lifetime mean GDP of the 2020 birth cohort are aligned with the population totals of newborns in 2020. Finally, we bin the ranked vulnerability indicators by their associated population totals into five groups of nearly equal population (as it is not possible to achieve perfect bin sizes given the sums of grid-scale population totals). This groups the richest and poorest and least and most deprived into the aforementioned quantile ranges. The quantile range of each vulnerability indicator is then a map that can be used to mask the existing locations of ULE, such as birth years and all GMT pathways. With GRDI (Supplementary Fig. 11) and GDP (Supplementary Fig. 12), we compare the lowest and the highest 20% of each indicator by population.

Data availability

The data for this analysis originate from multiple sources and are hereby listed. Model inputs, raw impact model simulations and post-processed extremes (the latter as Derived Output Data) from ISIMIP2b, as well as GDP data, are accessible at the ISIMIP repository here (<https://data.isimip.org>). Cohort sizes are taken from the Wittgenstein Centre for Demography and Global Human Capital (<https://dataexplorer.wittgensteincentre.org/wcde-v2>). Life expectancy data come from the UN demographics data portal (<https://population.un.org/dataportal/home?df=10750103-f8fa-4a7e-bb6a-b0f151970005>). Global mean temperatures are extracted from the AR6 scenario explorer⁴⁵ (<https://doi.org/10.5281/zenodo.7197970>). GRDI is hosted on the NASA EARTHDATA platform (<https://doi.org/10.7927/3xxe-ap97>). Maps in this analysis contain base map information made with Natural Earth (naturalearth-data.com).

Code availability

The code for this analysis can be found at GitHub (https://github.com/VUB-HYDR/2025_Grant_etal_Nature/tree/main).

30. Dunne, J. P. et al. GFDL's ESM2 global coupled climate-carbon Earth system models. Part I: physical formulation and baseline simulation characteristics. *J. Clim.* **25**, 6646–6665 (2012).

31. Jones, C. D. et al. The HadGEM2-ES implementation of CMIP5 centennial simulations. *Geosci. Model Dev.* **4**, 543–570 (2011).
32. Dufresne, J.-L. et al. Climate change projections using the IPSL-CM5 Earth System Model: from CMIP3 to CMIP5. *Clim. Dyn.* **40**, 2123–2165 (2013).
33. Watanabe, M. et al. Improved climate simulation by MIROC5: mean states, variability, and climate sensitivity. *J. Clim.* **23**, 6312–6335 (2010).
34. Russo, S., Sillmann, J. & Fischer, E. M. Top ten European heatwaves since 1950 and their occurrence in the coming decades. *Environ. Res. Lett.* **10**, 124003 (2015).
35. Russo, S., Sillmann, J. & Sterl, A. Humid heat waves at different warming levels. *Sci. Rep.* **7**, 7477 (2017).
36. Yamazaki, D., Kanae, S., Kim, H. & Oki, T. A physically based description of floodplain inundation dynamics in a global river routing model. *Water Resour. Res.* **47**, W04501 (2011).
37. Emanuel, K. Downscaling CMIP5 climate models shows increased tropical cyclone activity over the 21st century. *Proc. Natl Acad. Sci. USA* **110**, 12219–12224 (2013).
38. Holland, G. A revised hurricane pressure-wind model. *Mon. Weather Rev.* **136**, 3432–3445 (2008).
39. Klein Goldewijk, K., Beusen, A. & Janssen, P. Long-term dynamic modeling of global population and built-up area in a spatially explicit way: HYDE 3.1. *Holocene* **20**, 565–573 (2010).
40. Klein Goldewijk, K., Beusen, A. & Drecht, G. V. The HYDE 3.1 spatially explicit database of human-induced global land-use change over the past 12,000 years. *Global Ecol. Biogeogr.* **20**, 73–86 (2011).
41. Fricko, O. et al. The marker quantification of the Shared Socioeconomic Pathway 2: a middle-of-the-road scenario for the 21st century. *Global Environ. Change* **42**, 251–267 (2017).
42. Samir, K. C. & Lutz, W. The human core of the shared socioeconomic pathways: population scenarios by age, sex and level of education for all countries to 2100. *Global Environ. Change* **42**, 181–192 (2017).
43. Lutz, W., Goujon, A., Samir, K. C., Stonawski, M. & Stilianakis, N. (eds) *Demographic and Human Capital Scenarios for the 21st Century: 2018 Assessment for 201 Countries* (Publications Office of the European Union, 2018).
44. United Nations Department of Economic and Social Affairs. *World Population Prospects 2019* (United Nations, 2019).
45. Byers, E. et al. AR6 Scenarios Database v1.1. Zenodo <https://doi.org/10.5281/zenodo.7197970> (2022).
46. Murakami, D. & Yamagata, Y. Estimation of gridded population and GDP scenarios with spatially explicit statistical downscaling. *Sustainability* **11**, 2106 (2019).
47. Bartram, L. & Roe, B. Dependency ratios: useful policy-making tools? *Geriatr. Gerontol. Int.* **5**, 224–228 (2005).
48. Sharroff, D. et al. Global, regional, and national trends in under-5 mortality between 1990 and 2019 with scenario-based projections until 2030: a systematic analysis by the UN Inter-agency Group for Child Mortality Estimation. *Lancet Glob. Health* **10**, 195–206 (2022).
49. Smits, J. & Permanyer, I. The Subnational Human Development Database. *Sci. Data* **6**, 190038 (2019).
50. Laborde Debucquet, D. & Martin, W. Implications of the global growth slowdown for rural poverty. *Agric. Econ.* **49**, 325–338 (2018).
51. Bruederle, A. & Hodler, R. Nighttime lights as a proxy for human development at the local level. *PLoS One* **13**, e0202231 (2018).

Acknowledgements We acknowledge the Potsdam Institute for Climate Impact Research (PIK) for their coordination of ISIMIP and the modellers contributing runs to ISIMIP2b. We thank M. Andrijevic, C.-F. Schleussner and E. Byers for their discussions regarding this paper. W.T. acknowledges funding from the European Research Council (ERC) under the Horizon Framework research and innovation programme of the European Union (grant agreement no. 101076909; ERC Consolidator Grant LACRIMA). We acknowledge further funding from the European Union under the grant agreement no. 101081369 (SPARCCLIE). The computational resources and services used in this work were provided by the VSC (Flemish Supercomputer Center), funded by the Research Foundation – Flanders (FWO) and the Flemish Government, department EWI. This work was supported by the Wellcome Trust 309498/Z/24/Z.

Author contributions L. Grant helped to conceive this study, performed the analysis and wrote the paper. W.T. helped to conceive the study and write the paper. I.V. helped with coding parts of this analysis and writing the paper. L. Gudmundsson, E.F. and S.I.S. helped generate ideas for the analysis and curate the paper.

Competing interests The authors declare no competing interests.

Additional information

Supplementary information The online version contains supplementary material available at <https://doi.org/10.1038/s41586-025-08907-1>.

Correspondence and requests for materials should be addressed to Luke Grant.

Peer review information *Nature* thanks Stephane Hallegatte, Damon Matthews, Raya Muttarak, Dáithí Stone and the other, anonymous, reviewer(s) for their contribution to the peer review of this work.

Reprints and permissions information is available at <http://www.nature.com/reprints>.